Eur. Phys. J. D **29**, 49–56 (2004)
DOI: 10.1140/epjd/e2004-00011-9

THE EUROPEAN PHYSICAL JOURNAL D

Implantation of size-selected silver clusters into graphite

Linearity of implantation depth vs. scaled momentum

L. Seminara[a], P. Convers, R. Monot, and W. Harbich

Institut de Physique des Nanostructures, École Polytechnique Fédérale de Lausanne (EPFL), 1015 Lausanne, Switzerland

Received 21 August 2003 / Received in final form 24 November 2003
Published online 10 February 2004 –

Abstract. We report on a systematic study of the implantation of size-selected Ag_N^+ clusters on a graphite sample, for different cluster sizes ($N = 1, 3, 7, 9, 13$) and different impact energies ($E = 1{-}30$ keV). Results show that the implantation depth scales linearly with the *momentum* of the cluster, with a *stopping power* which depends on cluster size. We have particularly investigated the effects of the *size* and the *geometry* of the cluster on the implantation into the graphite substrate. A sort of *universal behavior*, which unifies different elements and different cluster geometries, can be recognized by scaling the momentum with the cluster projected surface. The *stopping power* of the cluster while penetrating the HOPG surface has been investigated for each cluster size, and a "molecular effect" is recognized, meaning that the stopping power is not additive in the number of atoms of the cluster.

PACS. 61.46.+w Nanoscale materials: clusters, nanoparticles, nanotubes, and nanocrystals – 68.55.Ln Defects and impurities: doping, implantation, distribution, concentration, etc. – 79.20.Rf Atomic, molecular, and ion beam impact and interactions with surfaces – 81.05.Uw Carbon, diamond, graphite

1 Introduction

The deposition of clusters preformed in the gas phase is an alternative route to the fabrication of controlled nanostructures. Size selection in these experiments is essential as has been shown for example in the recent progress on nanocatalysis [1, 2]. This type of experiments is typically performed in the "soft landing" regime, i.e. the clusters are deposited on the surface at very low energy in order to conserve the initial selected size. The cluster surface morphology generated in this way is generally quite unstable with temperature [3]. Exploitation of the controllable kinetic energy of the ionized cluster beam permits to pin the clusters to their impact point yielding much more stable structures. Creation of well-defined vertical nanostructures via implantation of clusters into a substrate [4] becomes possible.

The graphite surface is a model in the field of cluster physics [4–19]. Due to its unique layered structure it could be easily cleaned by cleavage and it is chemically inert. In particular, the impact of fullerenes [21, 22] and different ions [13, 23–27] on HOPG has been extensively studied, both by experiments and by molecular dynamics simulations.

In the last few years, the more complicated system of metal clusters on HOPG has also been modelled (by using quite different types of potentials describing the metal cluster and the covalently bonded graphite substrate) and experimentally analyzed.

In particular we are interested in the Ag_N/graphite system, for which significant progress has recently been reported [4–6, 8–10, 16, 17, 20]. For *low deposition* energies (i.e. <1 eV/atom), size-selected Ag clusters can diffuse and aggregate to create three-dimensional structures on the graphite substrate [11]. At *intermediate deposition* energies (i.e. $\approx 1{-}100$ eV/atom), above a threshold energy which scales with cluster size, deposited Ag_N clusters ($N = 50{-}200$) are pinned to their point of impact on the graphite surface [10]. Finally, for *high deposition* energies the Ag clusters implant into the graphite and rest at the bottom of a short tunnel [8]. The controlled creation of these well-defined nanostructured systems require a precise understanding of the scaling relations which define implantation. In particular, by molecular dynamics simulations the implantation of large Ag_N clusters ($N = 20{-}200$) is found to scale linearly [8] as $E/N^{\frac{2}{3}}$. On the other hand, recent results on the impact of smaller Ag_7 clusters on graphite indicate an implantation depth which scales with the *momentum* of the clusters. This scaling relation applies also to Au_7 and Si_7, suggesting an universal scaling behavior of the implantation depth for small clusters.

Moreover, in the case of small clusters, the cluster orientation and the impact site could be important parameters that affect the depth of cluster penetration.

[a] e-mail: lucia.seminara@epfl.ch

In this paper we present a systematic STM study of the implantation depth of (small) Ag_N clusters ($N = 1, 3, 7, 9, 13$) into graphite, for incoming kinetic energies ranging from 1 to 30 keV. For measurements of the implantation depth of the clusters, since the well-diameter is typically smaller than the STM tip, the sample is oxidized. Oxidation is used to obtain much wider etch pits of the same depth as the implanted cluster.

2 Experimental

2.1 Implantation of silver clusters into HOPG

The production of silver clusters has been performed with a CORDIS-type cluster source, based on sputtering of the Ag target with 20 keV Ar-ions [28]. Cations are extracted with a series of electrostatic lenses and filtered in energy by a Bessel-box (energy window of ± 7.5 eV). The silver ions Ag_N^+ are then injected into a quadrupole, and mass-selected (in this experiment $N = 1, 3, 7, 9, 13$). Mass-selected clusters are projected at normal incidence onto the graphite surface, which has been prepared by cleaving with Scotch tape immediately prior to insertion into vacuum. The profile of clusters impacts on the HOPG surface has approximately the form of a Gaussian distribution. The FWHM of the distribution depends on the distance between the quadrupole and the surface ($\simeq$1 cm), and on the bias voltage applied to the sample. The clusters impact energy is controlled by the voltage on the sample, and coverage is determined by the beam current density and the deposition time. Typical values of the beam current and of the deposition time are $\simeq$10 pA and $\simeq$5 s respectively, which yield a mean coverage of the order of 100 impacts/μm^2.

2.2 Oxidation

The cluster implantation depths are obtained by the etching method [4, 13, 18, 21, 29, 30]. The sample is treated in an oven, evacuated to a pressure of $\simeq 10^{-5}$ mbar, and heated to a temperature of 650 °C. A first annealing is performed in order to clean the sample (it is heated in vacuum at 650 °C for approximately 2 minutes). Oxidative etching is then achieved by heating the sample at the same temperature for approximately 25 minutes in a controlled atmosphere of oxygen (partial oxygen pressure is $\simeq$100 mbar).

Different etch times, temperatures and oxygen pressures control the pit growth rates and the activation energies [31]. In particular, the average diameter of the etched pits at a fixed temperature and oxygen pressure, increases linearly with reaction time [29].

2.3 STM

After oxidative etching, the sample is cooled down at ambient temperature, and examined by a "home-built" STM in air, which is based on the Pan design [32, 33]. Shear piezos allow the sample to move on the x-y plane, making displacements of the order of a few millimeters. The STM works in the "constant current mode", at ambient conditions of temperature and pressure. Images are taken at typical currents of the order of 1−2 nA and bias voltages of approximately 1−2 V (the sample is positively biased respect to the tip).

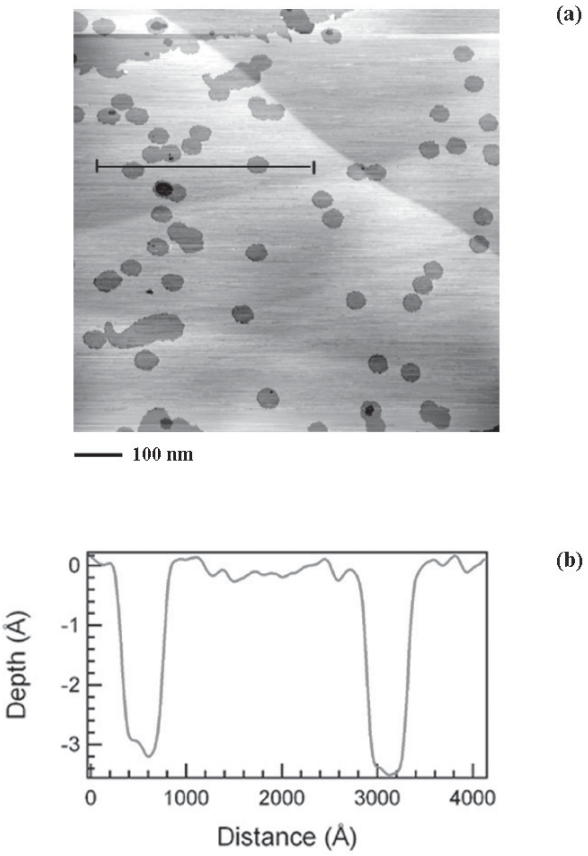

Fig. 1. (a) Etch pits generated on a pure HOPG sample heated at 650 °C in a 100 mbar atmosphere of oxygen for 40 min; (b) line scan on two different 1ML pits.

3 Results

3.1 Oxidative etching of pure HOPG

The results of the oxidation of the pure graphite substrate in a controlled atmosphere of approximately 100 mbar of oxygen, at 650 °C, is studied by *scanning tunneling microscopy*.

Figure 1 is a representative STM image showing etch pits of uniform size and monolayer depth formed on pre-existing defects in the HOPG basal plane. The density of pits in different samples varies from 80 to 100 μm^{-2}. Most of the defects are circular in shape, and their average diameter ranges about 40−50 nm. In a few cases, new etch pits are formed at the center of other pits. This possibly

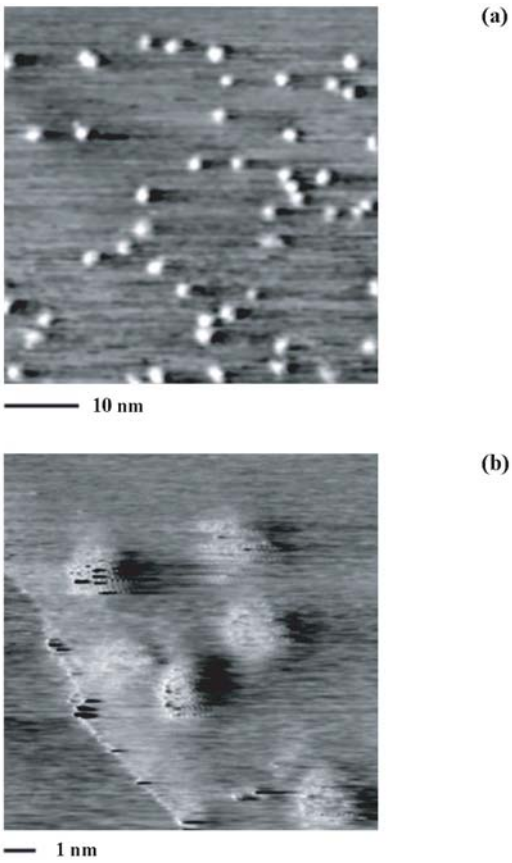

Fig. 2. (a) STM images of hillock defects on bombarded and still not oxidized HOPG surface; (b) zoom on implanted clusters.

happens where defects in the second layer are exposed to oxygen during the expansion of etch pits in the first layer.

These naturally occurring defects on the graphite surface, form a background of monolayer pits which is to be subtracted from the defects formed by cluster bombardment.

3.2 Implantation of Ag clusters into HOPG

3.2.1 Before oxidation

Figure 2 is a typical example of the graphite substrate after the implantation of Ag_7^+ clusters at a deposition energy of 2 keV. As such hillocks have never been observed on the pure HOPG surface, they constitute a mark of the presence of clusters on the substrate. Due to the small size of the protrusions, STM measurements *before* oxidation require a much higher impacts density than the usual one for the analysis of oxidized surfaces. In Figure 2 the coverage is approximately 20000 impacts/μm^2.

The mean hillocks diameter measures ≈20−30 Å and their mean height is approximately 3−4 Å. The size of the protrusions is the same as the one measured by the group of Palmer [14] for the implantation of Ag_N^+ ($N = 1, 3, 5, 7$) clusters on graphite, at similar impact energies. Protrusions of similar size are also observed in the case of different atomic ions impacting on graphite [34, 35].

3.2.2 After oxidation

After oxidation of the samples, hillocks are no longer visible but they are replaced by etch pits of various depths.

We have made a systematic study of the implantation depths of different Ag_N^+ clusters ($N = 1, 3, 7, 9, 13$) impacting on HOPG at energies ranging from 1 to 30 keV.

Figure 3 shows examples of the oxidized graphite surface after implantation of silver clusters of different sizes and different impact energies. All the images have been systematically analyzed by measuring the depth and the diameter of the etch pits. Each image contains two distributions: the first one due to clusters impacts on the surface, and the second one related to the one-monolayer natural defects. The etch pits associated to the naturally occurring defects are smaller and shallower than the pits originated from clusters impacts.

To obtain significant statistics, at least 80 pits have been measured, for each cluster size at a specific kinetic energy. Some of the results are shown in Figure 4. Almost all the depth distributions have a Gaussian form, once the background of monolayer pits coming from the natural graphite defects has been subtracted. Only the height-distribution associated to the implantation of monomers presents some differences, which will be described in Section 4.1.

By fitting the measured histograms with Gaussian distributions, we have determined the *mean implantation depth* for each cluster size at each incoming energy. In the case of the monomer, as the distribution is not Gaussian, the mean implantation depth is taken to correspond to the small peak appearing in the upper part of the distribution (for more details see Sect. 4.1).

Figure 5 contains the plots of the mean implantation depth (for each cluster size) as a function of the cluster incoming energy. If we consider the low energy range (Fig. 5b), the different curves are not easily distinguishable, even if error bars have been suppressed for more clarity. But when considering the whole energy range for Ag_7 and Ag_{13}, a "square-root" behavior of the mean depth as a function of energy can be recognized and possibly extended to the other sizes (Fig. 5a).

In the following sections, starting from this observed relation between the mean implantation depth and the cluster kinetic energy, the appropriate scaling relations connecting the depth to other dynamical parameters of the incident cluster will be explored.

4 Discussion of the results

4.1 Implantation of monomers

The monomer depth distribution does not take a Gaussian form, and the main peak corresponds to a pit depth

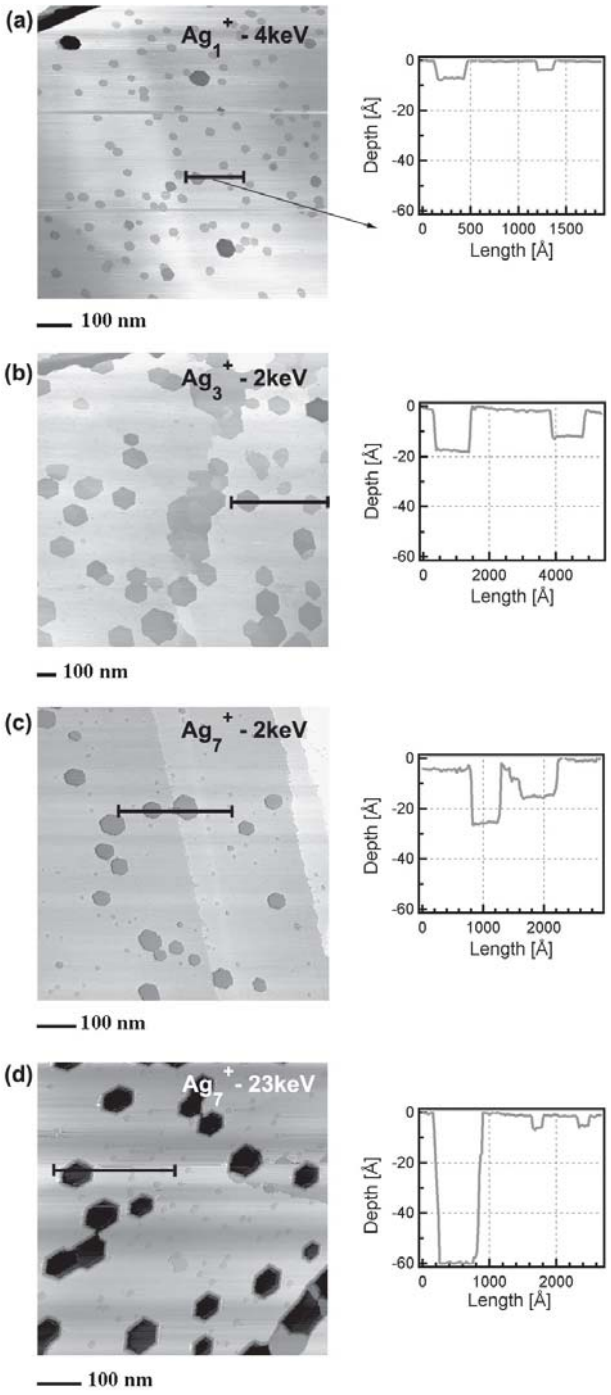

Fig. 3. Different examples of oxidized graphite surfaces, after the impact of Ag_N clusters at various kinetic energies.

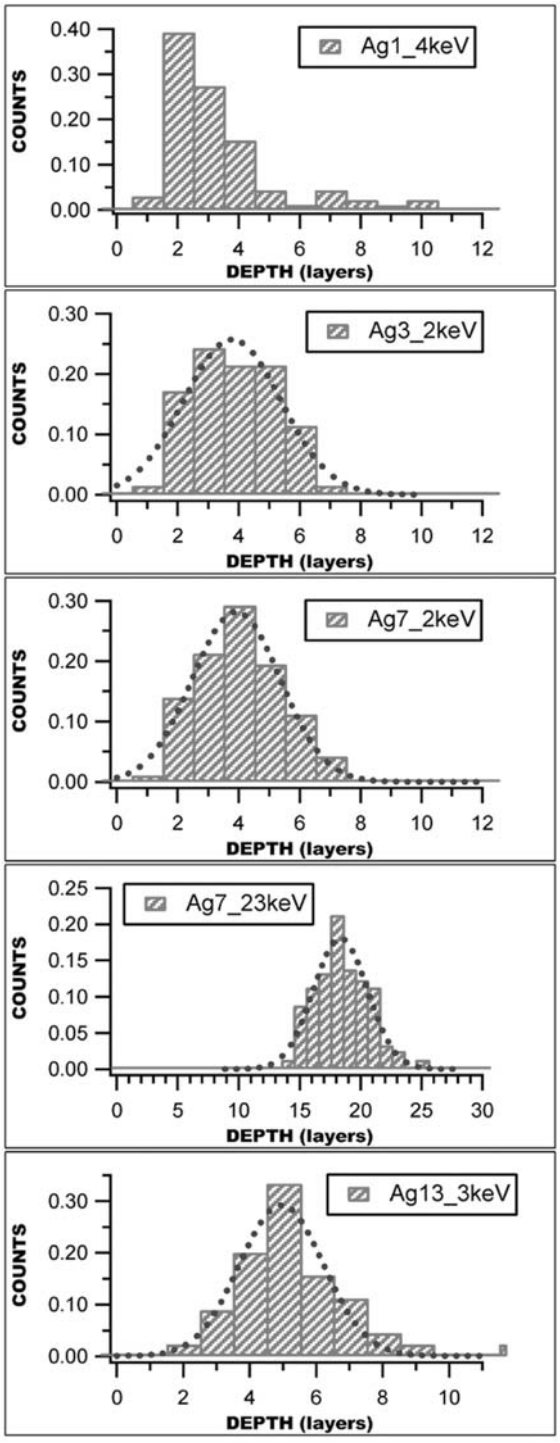

Fig. 4. Histograms of etch pit depths after implantation of Ag_N clusters at various kinetic energies, as measured by STM.

which is much shallower than the expected one. The possible reason is that, in the case of monomers, the distribution of etch pits depths doesn't reflect the implantation depth of the ions [27,36]. This is related to the fact that the monomer, due to its small size, can be trapped in-between graphite layers, forming *interstitial defects*. Both *vacancy defects* (VD) created by permanent displacement of surface carbon atom and interstitial defects (ID) are etched to pits, but their etching efficiencies are different [13]. Hahn and Kang have shown (for rare gases) that at all energies there is only a portion of the ID which is transformed into pits, while the rest of the ID defects vanishes without undergoing oxidative etching during the heating period [37]. On the other hand, nearly all carbon VD are converted to pits by thermal oxidation, for all the energies that we have considered.

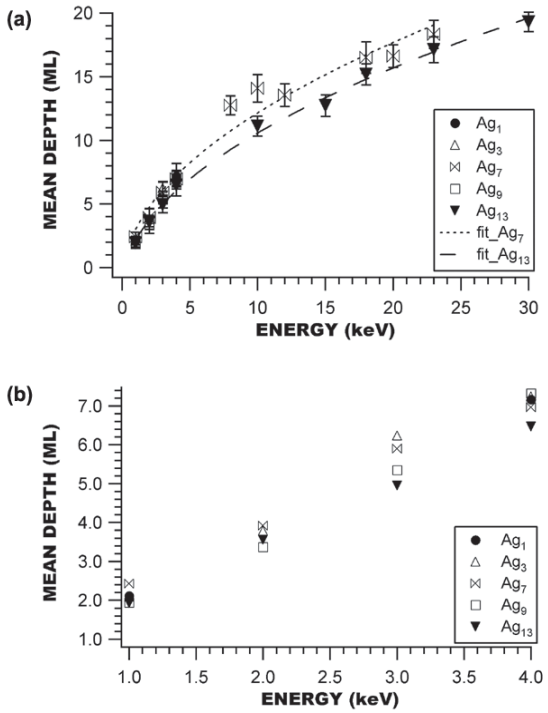

Fig. 5. Mean penetration depth as a function of the cluster incoming energy, for each cluster size. Filled and open marks are used, to better distinguish the different curves. In the following, our results will be characterized by filled marks. (a) The square-root fits of the Ag_7^+ and the Ag_{13}^+ curves are shown. Error bars have been added to the data points. (b) Zoom on the low-energy part of (a). Error bars have been suppressed for more clarity.

The low etching efficiency of interstitial defects can be explained by the following considerations. Energetic ions penetrate into HOPG producing line defects that cut through many layers. If there are no in-line defects in the upper layers just above the trapped ions, these buried defect sites are not accessible to the thermal oxidation by oxygen [27].

As in the case of the monomer implantation the proportion of interstitial defects can be important, the real penetration depth of the monomer ion is much higher than the peak of the measured pit-depths distribution. It is then reasonable to assume that the "real" mean implantation depth corresponds to the upper edge of the experimental pit-depths distribution.

4.2 Scaling relations

As cited in the introduction, recent results on the impact of Ag_7, Au_7 and Si_7 clusters on graphite, indicate an implantation depth which scales with the *momentum* of the clusters, suggesting an universal scaling behavior of the implantation depth for small clusters of different species. The linear relationship between the implantation depth and the cluster momentum is consistent with a retarding force proportional to the cluster velocity [17].

Interesting results come also from the study of fullerene cluster ion induced damage on HOPG, for impact energies ranging from 0.5 to 23 keV [22]. They fit their measured implantation depth with both a linear function of the incident velocity and the incident energy, and found a better description of the data with the first model [36].

Looking for a refined investigation of these recently proposed scaling relations, we made a systematic study on different silver cluster sizes ($N = 1, 3, 7, 9, 13$) impacting on HOPG over an extended energy range (from 1 to 30 keV).

Starting from the observed "square-root" behavior of the implantation depth vs. energy, we have found a good linear relation between the mean implantation depth and the cluster momentum (Fig. 6a). The results are presented for all cluster sizes and over the full energy range.

Trying to find a sort of "universal" behavior consisting in straight lines of same slope for each cluster size, we have tried to divide the momentum of the incoming cluster with the cluster projected surface. This momentum scaling was motivated by the fact that when we consider the outcome of cluster deposition, it is not only the energy or the momentum of the cluster which are important, but also the local area of the substrate with which the cluster interacts.

4.2.1 Scaled momentum in the approximation of spherical particles

We started by approximating clusters with spheres. The cluster volume is filled by N-atoms, which are treated like spheres. The atomic radius is the "Wigner Seitz radius", defined by the equation:

$$V = N\frac{4}{3}\pi r_{ws}^3 \quad \Rightarrow \quad r_{ws} = \sqrt[3]{\frac{3M_{at}}{4\pi\rho_0}} \tag{1}$$

in which ρ_0 is the density of the bulk, and M_{at} the mass of an element atom. For silver, r_{ws} is approximately 1.6 Å. In this approximation the cross-sectional area is equal to $\pi N^{\frac{2}{3}} r_{ws}^2$. In the case of the monomer ion, we consider that it is neutralized before the impact on the graphite surface. It is then treated like a neutral atom.

Dividing the momentum of the N-atoms cluster by $N^{\frac{2}{3}} r_{ws}^2$, we obtain a momentum scaled by the cluster projected surface. In Figure 6b the mean implantation depth is plotted as a function of this scaled momentum. The curves are presented only up to an energy of 4 keV, in order to consider the same energy range for all cluster sizes, and to have higher visibility on the different curves. Results on C_{60}^+ [22] are added for comparison.

C_{60}^+ is taken with its own real structure, a sphere of radius 5.6 Å. The C_{60}^+ projected surface is then the section of the sphere.

Observing the graph, we can conclude that this approximation is already quite good. All the curves group together (except for C_{60}^+), and there is a good accordance between the slopes of the different straight lines.

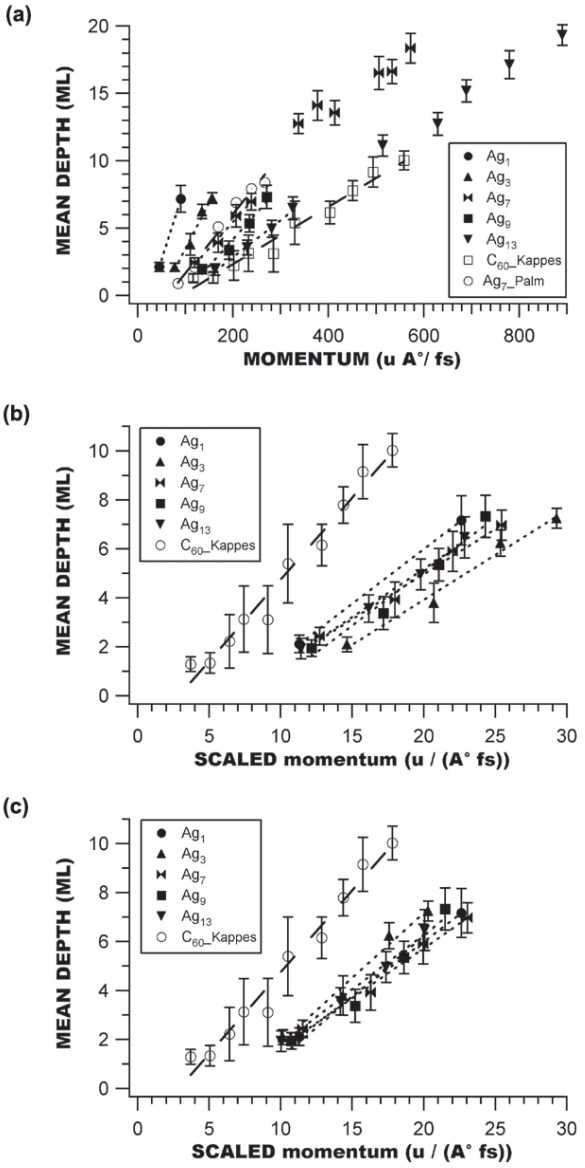

Fig. 6. (a) Mean penetration depth vs. momentum, for the different cluster sizes over the full energy range (filled marks). Results on C_{60}^+ [22] and on Ag_7^+ [17] are added for comparison (open marks). For the data on Ag_7^+ by the Palmer group, the plotted implantation depth corresponds to the upper edge of the experimental distribution. (b) The momentum is scaled with the cluster projected surface, in the approximation of *spherical particles*. Results on C_{60}^+ [22] are added for comparison. (c) The momentum is scaled with the projected surface calculated from the *real cluster geometry*. Results on C_{60}^+ are added for comparison [22].

4.2.2 Scaled momentum starting from the calculated geometry of the cluster

Trying to obtain an even better description of the problem, we have calculated the cluster projected surface starting from the geometrical structure of the clusters (Fig. 7). The monomer is still treated like a sphere whose radius is the Wigner-Seitz radius.

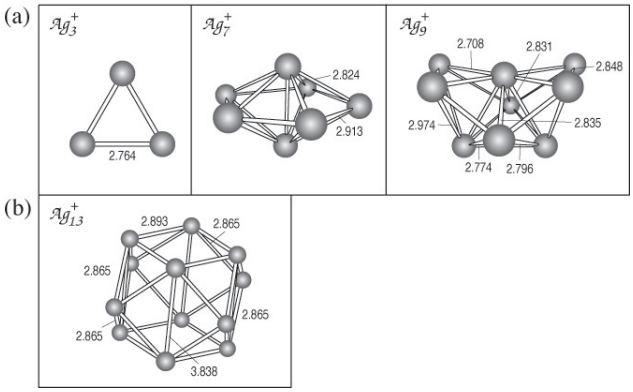

Fig. 7. (a) Geometry of Ag_N^+ ($N = 3, 7, 9$) clusters as calculated by Bonačić-Koutecký [41]; (b) geometry of Ag_{13}^+ as calculated with a DFT scheme by Dr. Fortunelli, CNR of Pisa, Italy [42]. In its ground structure, Ag_{13}^+ is a distorted "Jahn-Teller" cuboctahedron.

Except for Ag_1^+ and for Ag_3^+ (whose case will be discussed later), the size of the atoms is considered to be negligible for the calculation of projected surfaces, and atoms are treated like points. Obviously, this approximation is reasonable only for large sizes (cluster projected surface $\gg$ "atom projected surface"). Still in the case of "large" clusters, the projected surface is calculated as the arithmetical mean between the maximal and minimal sections. This approximation improves as higher the symmetry of the clusters is, and it takes into account all the possible orientations into which the cluster can hit the surface. In the case of large clusters we neglect (as first approximation) the deformation of the cluster when it impacts on the HOPG substrate.

We shall now discuss the case of the trimer ion, which has a planar structure (Fig. 7a). As the atomic dimensions are of the same order of the triangular surface calculated from the interatomic distances, atoms cannot be considered as points. In a good approximation, we can assume that atoms are arranged in the plane in order to fill the triangular structure. If at the impact on the HOPG substrate the Ag_3^+ plane and the graphite surface are parallel, the cluster is not deformed and the projected surface is simply equal to three times the "atomic section", πr_{ws}^2. In the case of all the other orientations of the impinging cluster respect to the graphite plane, we imagine that the rear atom feels the repulsive potential of the other two, the cluster rotates and hits the surface in the same configuration than before. Ag_3^+ "mean" projected surface is then equal to three times the "atomic section".

Results obtained with this more accurate momentum scaling are shown in Figure 6c. We can observe that all curves group together, and the slope is almost identical to the C_{60}^+ one (the curve associated to C_{60}^+ doesn't change with respect to the previous model, as it is in both cases taken with its own real spherical structure). The good agreement obtained proves that, independently on the considered element and on the cluster geometry, implantation depth is a linear function of a momentum "per unit surface".

4.3 Stopping power

Fitting the linear behavior of the implantation depth as a function of cluster *velocity*, we found different straight lines for different cluster sizes (we have shown the linear dependence between implantation depth and cluster *momentum* in Sect. 4.2):

$$h = a_N + b_N v_0 \tag{2}$$

where h is the mean implantation depth expressed in meters ([m]), a_N and b_N are the fit parameters of the straight lines(expressed in [m] and [s], respectively), and v_0 is the initial velocity of the cluster.

As Pratontep et al. [17] pointed out, the latter equation is consistent with a linear dependence of cluster velocity v on distance x from the surface, arising from the application of Newton's Law with a Stoke's type resistance force.

We can then derive the initial cluster kinetic energy E_0 in terms of the initial cluster velocity, v_0, to find:

$$E_0 = \frac{m}{2}\frac{h^2}{b_N^2} - \frac{ma_N}{b_N^2}h + \frac{ma_N^2}{2b_N^2}.$$

We can assume that the latter quantity, with $h = x$, equals the loss of energy undergone by the cluster at a distance x from the surface. In other words, we can express the energy of the cluster at "distance x" in the form:

$$E = E_0(h) - E_0(x).$$

The *stopping power* is defined by dE/dx, the energy loss per unit distance, which means:

$$\frac{dE}{dx}(x) = \frac{m}{b_N^2}x - \frac{ma_N}{b_N^2}. \tag{3}$$

Significant is the trend of the stopping power as a function of cluster velocity, for each cluster size. In equation (3) we can insert the mentioned linear behavior of x vs. v using equation (2), and obtain:

$$\frac{dE}{dx}(x) = \frac{m}{b_N^2}(a_N + b_N v_0) - \frac{ma_N}{b_N^2} = \frac{m}{b_N}v_0. \tag{4}$$

This equation shows that the stopping power varies linearly with the incident velocity, with a slope which changes with the cluster size.

A consequence of the linear behavior of the implantation depth as a function of the cluster momentum is that the stopping power S shows a so-called *molecular effect*, i.e.:

$$S(N) \propto N^{\alpha} S(1) \tag{5}$$

with $\alpha < 1$.

All the "stopping power vs. velocity" curves have been scaled with the stopping power associated to the monomer, $S(1)$. The resulting curve $(S(N)/S(1))$ is shown in Figure 8, together with the fitting curve $\beta N^{\frac{2}{3}}$, with $\beta = 0.73 \pm 0.03$. Analyzing our data yields a good agreement with the fit $N^{\frac{2}{3}}$, which relates the term N^{α} (Eq. (5)) to the projected surface in the sphere model.

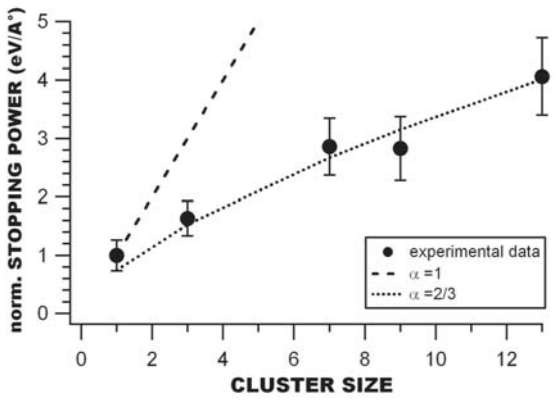

Fig. 8. Stopping power normalized with the curve associated to the monomer. Two different N^{α} curves are shown ($\alpha = 1$: no molecular effect, $\alpha = 2/3$: projected surface in the sphere model).

This "molecular behavior" is consistent with previously reported results [38–40], obtained both in the case of heavy ions incident on a light target and in the case of a mass ratio equal to one. This phenomenon is explained by assuming that the earlier arriving cluster atoms knock out the target atoms and *clear the way* for the late-coming cluster atoms [38].

5 Conclusions

In summary, we have reported a systematic study on the implantation of silver clusters into a graphite substrate, for different cluster sizes and over an extended energy range.

First we have found a linear dependence between the *penetration depth* and the *momentum* of the cluster, for each cluster size. This result is in good accordance with previous results for the impact of C_{60}^+, Ag_7^+ and Au_7^+ on the same substrate.

In particular we have investigated the effects of the cluster *geometry* on the implantation into the graphite substrate. The step from the simple liquid drop model to the actual calculated geometry of the cluster improved considerably the model.

Finally we have investigated the stopping power "felt" by the Ag clusters of different sizes, while penetrating the HOPG substrate. An important question is whether the stopping power is simply linear with the number of atoms N in the cluster. Data clearly show a *molecular behavior*, meaning that the stopping power per cluster atom is smaller than the stopping power for atomic projectiles moving at the same velocity. In particular, we were able to quantify this molecular effect.

The authors would like to thank Dr. H. Hövel for helpful discussions about the process of oxidation of graphite, and Dr. A. Fortunelli for the calculation of the geometric structure of Ag_{13}^+. The authors are also very grateful to R.E. Palmer for all the comments, suggestions and useful discussions about

this manuscript. This work has been supported by the Swiss National Science Foundation.

References

1. U. Heiz, W.D. Schneider, J. Phys. D: Appl. Phys. **33**, R85 (2000)
2. U. Heiz, W.D. Schneider, Crit. Rev. Sol. St. Mat. Sci. **26**, 251 (2001)
3. R. Schaub, H. Jödicke, F. Brunet, R. Monot, J. Buttet, W. Harbich, Phys. Rev. Lett. **86**, 3590 (2001)
4. D.J. Kenny, S. Weller, M. Couillard, R.E. Palmer, C.F. Sanz-Navarro, R. Smith, Eur. Phys. J. D **16**, 115 (2001)
5. S.J. Carroll, S.G. Hall, R.E. Palmer, R. Smith, Phys. Rev. Lett. **81**, 3715 (1998)
6. S.J. Carroll, K. Seeger, R.E. Palmer, Appl. Phys. Lett. **72**, 305 (1998)
7. S.J. Carroll, P. Weibel, B.v. Issendorff, L. Kuipers, R.E. Palmer, J. Phys.: Condens. Matter **8**, L617 (1996)
8. S.J. Carroll, P.D. Nellist, R.E. Palmer, S. Hobday, R. Smith, Phys. Rev. Lett. **84**, 2654 (2000)
9. S.J. Carroll, R.E. Palmer, P.A. Mulheran, S. Hobday, R. Smith, Appl. Phys. A **67**, 613 (1998)
10. S.J. Carroll, S. Pratontep, M. Streun, R.E. Palmer, S. Hobday, R. Smith, J. Chem. Phys. **113**, 7723 (2000)
11. I.M. Goldby, L. Kuipers, B.v. Issendorff, R.E. Palmer, Appl. Phys. Lett. **69**, 2819 (1996)
12. C.M. Grimaud, R.E. Palmer, J. Phys.: Condens. Matter **13**, 1869 (2001)
13. J.R. Hahn, H. Kang, Surf. Sci. **446**, L77 (2000)
14. S.G. Hall, M.B. Nielsen, R.E. Palmer, J. Appl. Phys. **83**, 733 (1998)
15. B. Kaiser, T.M. Bernhardt, K. Rademann, Appl. Phys. A **66**, S711 (1998)
16. D.J. Kenny, R.E. Palmer, C.F. Sanz-Navarro, R. Smith, J. Phys.: Condens. Matter **14**, 185 (2002)
17. S. Pratontep, P. Preece, C. Xirouchaki, R.E. Palmer, C.F. Sanz-Navarro, D.J. Kenny, R. Smith, Phys. Rev. Lett. **90**, 055503 (2003)
18. C.T. Reimann, S. Andersson, P. Bruhwiler, N. Martensson, L. Olsson, R. Erlandosson, M. Henkel, H.M. Urbassek, Nucl. Instrum. Meth. Phys. Res. B **140**, 159 (1998)
19. C.F. Sanz-Navarro, R. Smith, D.J. Kenny, S. Pratontep, R.E. Palmer, Phys. Rev. B **65**, 1 (2002)
20. W. Yamaguchi, K. Yoshimura, Y. Tai, Y. Maruyama, K. Igarashi, S. Tanemura, J. Murakami, J. Chem. Phys. **112**, 9961 (2000)
21. G. Bräuchle, S.R. Schneider, D. Illig, J. Rockenberger, R.D. Beck, M.M. Kappes, Appl. Phys. Lett. **67**, 52 (1995)
22. G. Bräuchle, S.R. Schneider, D. Illig, R.D. Beck, H. Schreiber, M.M. Kappes, Nucl. Instrum. Meth. Phys. Res. B **112**, 105 (1996)
23. J.R. Hahn, H. Kang, Surf. Sci. **357-358**, 165 (1996)
24. S.M. Lee, Y.H. Lee, Y.G. Hwang, J.R. Hahn, H. Kang, Phys. Rev. Lett. **82**, 217 (1999)
25. D. Marton, H. Bu, K.J. Boyd, S.S. Todorov, A.H. Al-Bayati, J.W. Rabalais, Surf. Sci. **326**, L489 (1995)
26. C.T. Reimann, P.A. Sullivan, A. Turpitz, S. Altmann, A.P. Quist, A. Bergman, S.O. Oscarsson, B.U.R. Sundqvist, P. Hakansson, Surf. Sci. **341**, L1019 (1995)
27. Y.-J. Zhu, T.A. Hansen, S. Ammerman, J.D. McBride, T.P. Beebe, J. Phys. Chem. B **105**, 7632 (2001)
28. G. Vandoni, C. Félix, R. Monot, J. Buttet, W. Harbich, Chem. Phys. Lett. **229**, 51 (1994)
29. H. Chang, A.J. Bard, J. Am. Chem. Soc. **113**, 5588 (1991)
30. X. Chu, L.D. Schmidt, Carbon **29**, 1251 (1991)
31. F. Stevens, L.A. Kolodny, T.P. Beebe, J. Phys. Chem. B **102**, 10799 (1998)
32. S.H. Pan, *International Patent Publication Number WO 93/19494* (international Bureau, World Intellectual Property Organization, 1993)
33. S.H. Pan, E.W. Hudson, J. Davis, Rev. Sci. Instrum. **70**, 1459 (1999)
34. R. Coratger, A. Claverie, A. Chahboun, V. Landry, F. Ajustron, J. Beauvillain, Surf. Sci. **262**, 208 (1992)
35. T. Li, B.V. King, R.J. MacDonald, G.F. Cotterill, D.J. O'Connor, Q. Yang, Surf. Sci. **312**, 399 (1994)
36. S. Gilb, M. Blom, G. Bräuchle, C. Stoermer, R. Wellmann, M.M. Kappes (not published)
37. J.R. Hahn, H. Kang, J. Vacuum Sci. Technol. A **17**, 1606 (1999)
38. V.I. Shulga, P. Sigmund, Nucl. Instrum. Meth. Phys. Res. B **47**, 236 (1990)
39. V.I. Shulga, Nucl. Instrum. Meth. Phys. Res. B **58**, 422 (1991)
40. Z. Pan, Nucl. Instrum. Meth. Phys. Res. B **66**, 325 (1992)
41. V. Bonacić-Koutecky, L. Cespiva, P. Fantucci, J. Koutecky, J. Chem. Phys. **98**, 7981 (1993)
42. A. Fortunelli (private communication)